

Interface characterization of $\text{Co}_2\text{MnGe}/\text{Rh}_2\text{CuSn}$ Heusler multilayers

Ronny Knut,¹ Peter Svedlindh,² Oleg Mryasov,³ Klas Gunnarsson,² Peter Warnicke,⁴
Dario Arena,⁴ Matts Björck,¹ Andrew Dennison,⁵ Anindita Sahoo,^{6,7} Sumanta
Mukherjee,⁷ D.D. Sarma,⁷ Sari Granroth,⁸ Mihaela Gorgoi,⁹ and Olof Karis¹

¹*Department of Physics and Astronomy,
Uppsala University, Box 516, 75120 Uppsala, Sweden*

²*Solid State Physics, Department of Engineering Sciences, Uppsala University*

³*Department of Physics and Astronomy and
MINT Center, University of Alabama, Tuscaloosa*

⁴*National Synchrotron Light Source Brookhaven
National Laboratory Upton, New York 11973, USA*

⁵*Institut Laue-Langevin, Grenoble 38042, France*

⁶*Department of Physics, Indian Institute of Science, Bangalore-560 012, India*

⁷*Solid State and Structural Chemistry Unit,
Indian Institute of Science, Bangalore-560 012, India*

⁸*Department of Physics, University of Turku, Finland*

⁹*Helmholtz Zentrum Berlin für Materialien und Energie GmbH, BESSY II, Berlin, Germany*

(Dated: May 28, 2022)

Abstract

All-Heusler multilayer structures have been investigated by means of high kinetic x-ray photoelectron spectroscopy and x-ray magnetic circular dichroism, aiming to address the amount of disorder and interface diffusion induced by annealing of the multilayer structure. The studied multilayers consist of ferromagnetic Co_2MnGe and non-magnetic Rh_2CuSn layers with varying thicknesses. We find that diffusion begins already at comparably low temperatures between 200 °C and 250 °C, where Mn appears to be most prone to diffusion. We also find evidence for a 4 Å thick magnetically dead layer that, together with the identified interlayer diffusion, are likely reasons for the small magnetoresistance found for current-perpendicular-to-plane giant magneto-resistance devices based on this all-Heusler system.

I. INTRODUCTION

Magnetic read head technology has experienced several large paradigm changes during the last 15 years. Anisotropic magnetoresistance read heads were surpassed by read heads based on giant magnetoresistance (GMR) in 1996 enabled by the Nobel-awarded findings of Grünberg and Fert^{1,2}. Very soon after the discovery of tunnel magneto-resistance (TMR), record values of the magnetoresistance (MR) were reported for sensors based on this effect. Today, TMR structures require a very thin MgO tunneling barrier (typically ~ 1 nm) to achieve a sufficiently low resistance of the device and further significant decrease of the barrier thickness appears unrealistic. It has been suggested that current-perpendicular-to-plane (CPP) GMR structures, as opposed to current in-plane structures used in the first generation GMR devices, are candidates to become the next generation of MR sensors as they do not suffer resistance issues due to the all-metallic design³.

Heusler alloys are ternary alloys with the composition X_2YZ , where X and Y in general are two different transition metal atoms and Z is a group 3 or 4, non-metallic element. A half-metallic character, i.e. that the density of states of the majority band is metallic while the minority band exhibits a gap at the Fermi level, was theoretically predicted for the ferromagnetic (FM) half-Heusler alloy NiMnSb⁴ followed by the extensive investigation of properties originating from this remarkable feature of the electronic structure⁵. This Heusler alloy was investigated as a candidate material for a novel CPP-GMR structure with Cu as spacer layer⁶. Recently, Co based full-Heusler alloys renewed the interest for this topic. Experimental results for two types of non-magnetic (NM) spacers have been reported fairly recently; (i) elemental metal spacers^{7,8} with (001) texture and (ii) non-magnetic Heusler alloy spacers⁹⁻¹¹ with (110) texture. Combinations of the (001) textured FM Heusler alloys Co_2MnSi and $\text{Co}_2\text{Fe}(\text{Si}_{0.5}\text{Al}_{0.5})$ with Ag yielded MR values in excess of 28% and a change in the resistance-area product (ΔRA) of $8.8 \text{ m}\Omega \cdot \mu\text{m}^2$.^{7,8} More recently, enhancement of CPP-GMR up to 70% MR and a ΔRA of $16.8 \text{ m}\Omega \cdot \mu\text{m}^2$ have been measured for $\text{Co}_2(\text{Fe}_{0.4}\text{Mn}_{0.6})\text{Si}$ electrodes with (001) Ag as spacer.¹²

The half-metallic character has been theoretically predicted for ideal L2_1 crystals. For actual samples a certain amount of disorder is expected, which will have a negative impact on the value of the spin polarization¹³⁻¹⁷. The CPP-GMR in all-Heusler structures can be affected by different types of disorder, including bulk FM, bulk NM disorder and disorder

specific to FM/NM interfaces. Ambrose and Mryasov^{9,10} proposed a combination of FM and NM Heusler alloys to maximize the spin asymmetry at the FM/NM interface. They argue that a structure with the appropriate combination of FM and NM Heusler alloys could provide a large, spin dependent, interface contribution to the magnetoresistance^{9,10}, which, due to the non-Stoner like spin-splitting in the FM Heusler will be less sensitive to disorder.¹¹

For device fabrication, due to compatibility with existing processes, it would be advantageous to use the (110) textured combination of Co₂MnGe (CMG) and the non-magnetic Heusler alloy Rh₂CuSn (RCS)^{9,10}. A prototype hard disk drive reader with a MR of about 7% and a Δ RA of about $4.0 \text{ m}\Omega \cdot \mu\text{m}^2$ has been constructed by Nikolaev et al.¹¹ using such considerations. However, it is still much lower than for TMR structures and too low for being a viable alternative in sensor technology where MR ratios in the range of 50% at Δ RA products in the order of $0.1 \Omega \cdot \mu\text{m}^2$ are considered to be required in the roadmap for magnetic media beyond 2TBit/inch².³

In this work, we have studied the FM/NM interfaces in all-Heusler multilayer structures. The work focuses on changes induced by post-growth low temperature annealing and it is shown that diffusion of atomic species is initiated already in the temperature range between 200 °C and 250 °C.

II. EXPERIMENT

We have studied multilayer samples comprised of the full-Heusler compound CMG as the magnetic layer between non-magnetic layers of the full-Heusler RCS. The samples were grown using a commercial magnetron sputtering system (Canon Anelva C7100)¹¹. The aim of this study is to understand the effects of post-growth annealing on interface quality and how these depend on the individual layer thicknesses. The magnetic properties and in particular the quality of the interfaces are studied using x-ray magnetic circular dichroism (XMCD)^{18,19}, polarized neutron reflectivity and SQUID magnetometry. The modifications of the interfaces were characterized by means of hard x-ray photoelectron spectroscopy (HAX-PES or HX-PES, also commonly referred to as HIKE for high kinetic energy photoelectron spectroscopy)²⁰⁻²². Additional characterizations using ferromagnetic resonance and x-ray resonant magnetic scattering have also been performed and will be published elsewhere²³.

The XMCD experiments were performed at beamlines I1011 and D1011 at the synchrotron facility MAX-lab in Lund, Sweden, with 90% and 75% circularly polarized light, respectively. All data were obtained using total electron yield. The samples were magnetized in-plane after which they were measured in remanence at room temperature. The HAXPES measurements were conducted using the HIKE station²² at the KMC-1 beamline of the BESSY II synchrotron facility at Helmholtz Zentrum Berlin, Germany. The samples were heated to different temperatures in the range 200 °C - 500 °C at a constant rate of 10 °C/min and kept at constant temperature for 10 min, after which the samples were cooled down to room temperature (RT) before a measurement.

Polarized neutron reflectivity were conducted up to the first Bragg peak at the Super-Adam instrument at the Institut Laue-Langevin. The instrument was operated with a highly oriented pyrolytic graphite monochromator and two Bragg mirrors to polarize the incident beam, producing an incident wavelength of 4.4 Å. The reflected beam was analysed with a supermirror. After each measurement the sample was annealed at the next temperature for 1 h under vacuum and was subsequently allowed to oven cool during half a day. Note that the heating protocol used for the neutron measurements is different to the one used for the other measurements primarily due to the available hardware at the different facilities. As diffusion is found to be present already at the lowest temperatures used (100 °C), we expect that the neutron data are representative of a further progressed diffusion process, when compared to data obtained in the other measurements for the same annealing temperature. In Table I, we list the samples used in this study. The samples have different combinations of CMG and RCS layers thicknesses. Three of the samples are given descriptive names since these are the most extensively studied, while the other samples will be explicitly denoted when discussed.

III. RESULTS

Regularly, beamlines dedicated to photoemission seldom offer photon energies above 1 keV with reasonable photon intensity and resolution, which limits the electron mean free path to about 5 Å. The KMC-1 beamline at HZB delivers 2 - 12 keV photons with high resolution, making it ideal for studying bulk properties²⁰⁻²². All the photoemission results described here have been obtained using a photon energy of 4 keV giving an estimated

TABLE I. Sample annotations and thicknesses of CMG and RCS layers.

Annotation	CMG (\AA)	RCS (\AA)
Thick non-magnetic layer	6	18
Thick magnetic layer	18	6
Thick layers	18	18
-	24	18
-	18	12
-	18	12

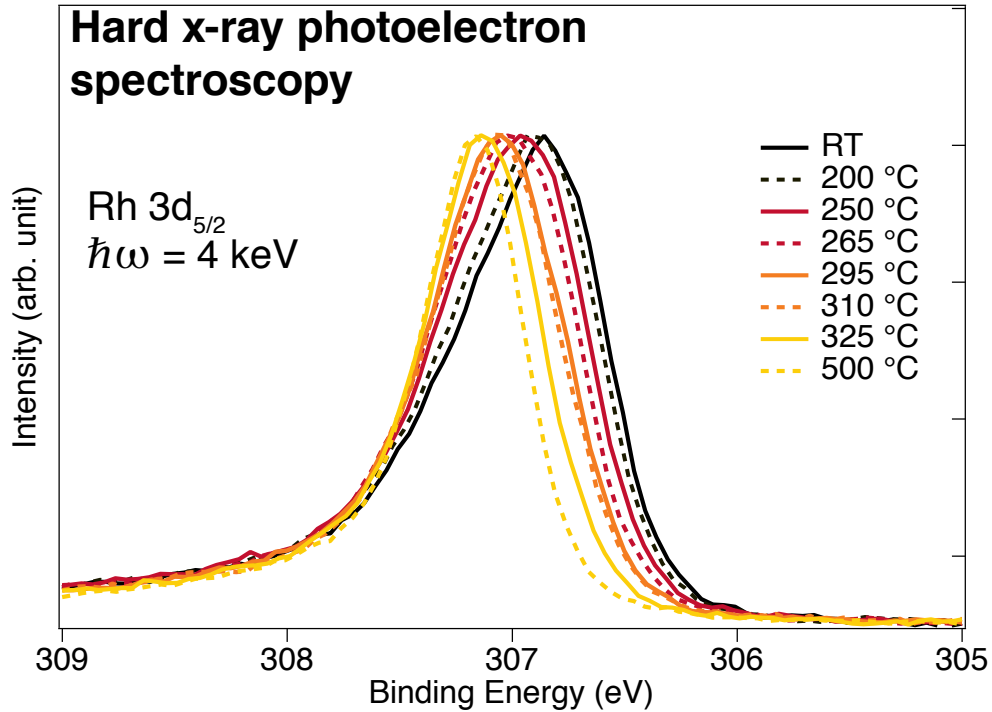


FIG. 1. (Color online) Photoemission of Rh $5d_{5/2}$ from sample CMG 18\AA /RCS 18\AA (hereafter denoted 'Thick layers') after different annealing temperatures. There is a peak shift to higher binding energy with increasing annealing temperature. The spectrum obtained for 265 °C (red dash-dotted line) has been deconvoluted in Fig. 2.

electron mean free path of 50 Å.

As an atom in a solid is ionized by photons, the system will adapt to the presence of the positively charged ion by screening of the same. In general this involves both inter-atomic screening and intra-atomic relaxation. In metallic systems, a substantial fraction of the screening is due to mobile conduction electrons. The effectiveness of the screening will affect the kinetic energy of the photoelectron and hence also the measured binding energy of that electron. The screening of the ionized atom depends on the nature of electronic structure of the local environment and the hybridization between the ionized atom and its surrounding. This is known as the chemical shift in core level spectra²⁴. We use this fact to distinguish between bulk and interface atoms and study how these are affected by annealing.

The sample with the thick CMG and RCS layers has been studied for several annealing temperatures between 200 °C and 500 °C, while the thick non-magnetic layer and thick magnetic layer samples have been measured for a few selected annealing temperatures. The Rh 5d_{5/2} photoemission core level is shown in Fig. 1 for the sample denoted 'Thick layers' (conf. Table I). The peak clearly moves to higher binding energy (BE) with increasing annealing temperature. It is relatively speaking easy to acquire this core level with good statistics. In combination with the large chemical shifts found for this Rh core level, makes it possible to reliably fit the spectra with multiple peaks, as illustrated in Fig. 2. All lineshapes are set to Doniac-Sunjic type²⁵, where the asymmetry and peak broadening are kept constant for every core level and chosen so that the experimental BE shift can be well described with as few peaks as possible. A Shirley-type background was used in the fit.²⁶

Each spectrum is fitted with three main peaks; one component at 306.78 eV, one at 306.98 eV, and one at 307.14 eV binding energy, respectively. A fourth peak at high BE (307.36 eV) appears to be related to the two main peaks at the lower BE side, since its intensity is always 14% of these peaks. A common disorder in the full X₂YZ Heusler is X antisites in the Y atomic position. Thus, Rh anti-sites is a plausible explanation for this high BE peak, since it is not unlikely that 14% disorder of this type can occur²⁷. As the Rh begins to migrate due to heating, the disorder is cured at the same rate.

The intensities of the three main peaks a function of temperature, obtained by spectral deconvolution as described above as, are plotted in Fig. 3. To better describe and understand the origin of these three peaks we performed Monte Carlo simulations, where the change of the coordination number, i.e. the number of Rh nearest neighbors (NN), was studied when

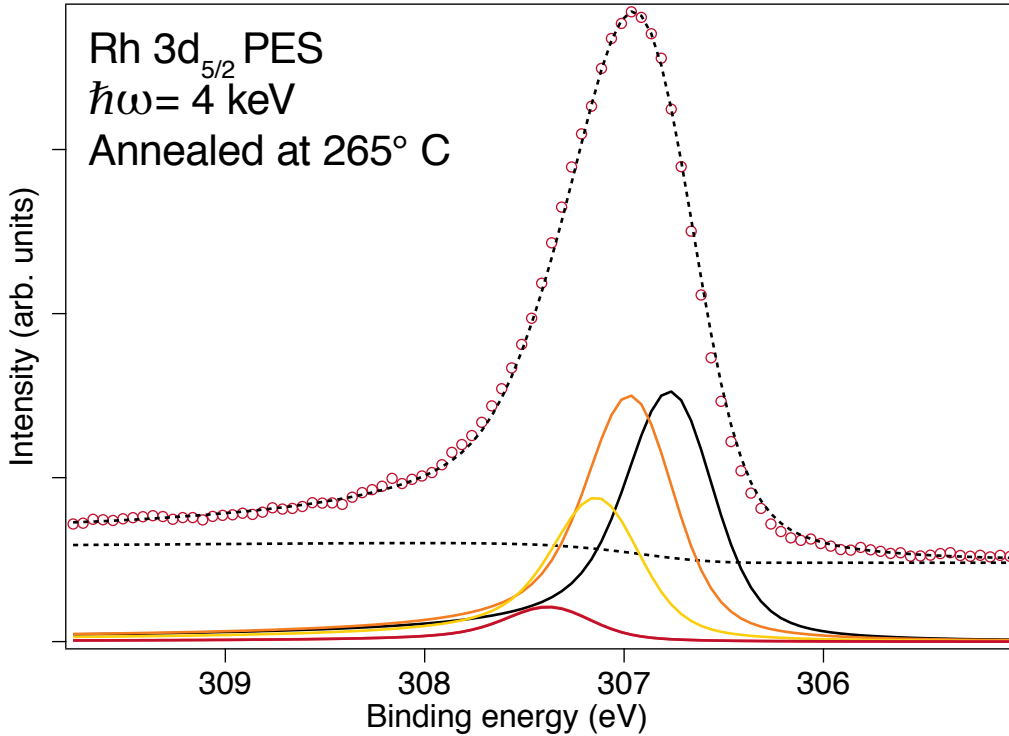


FIG. 2. (Color online) Deconvoluted spectrum of the Rh $3d_{5/2}$ core level, fitted with 3 main peaks and a peak at the high BE shoulder, which is always 14% of the two main peaks at the lower BE side.

introducing random disorder as a consequence of heat treatment. The BE shift is most sensitive to the number of Y and Z atoms Rh has as NN, and not to the Rh NN, which are actually the next nearest neighbors. We made the assumption that the composition of NNs is reflected in the number of Rh neighbors. In reality, the Rh atoms occupy two fcc lattices in this Heusler compound, which corresponds to a simple cubic structure with 6 NN. This structure did not give a good fit to the experimental results since the number of Rh NN is too small to encompass all combinations of realistic NN configurations. Instead we considered the next nearest neighbors and assumed that the Rh were coordinated to 12 Rh neighbors, i.e. a local fcc-coordination of Rh.

A $26 \times 26 \times 26$ lattice was constructed with two layers of Rh atoms, each 12 monolayers (ML) thick, representing the RCS layers. The diffusion of Rh atoms was simulated by generating random numbers (in the range 0 - 1) that should be smaller than $\exp\left[-\frac{E}{k_B T}\right]$,

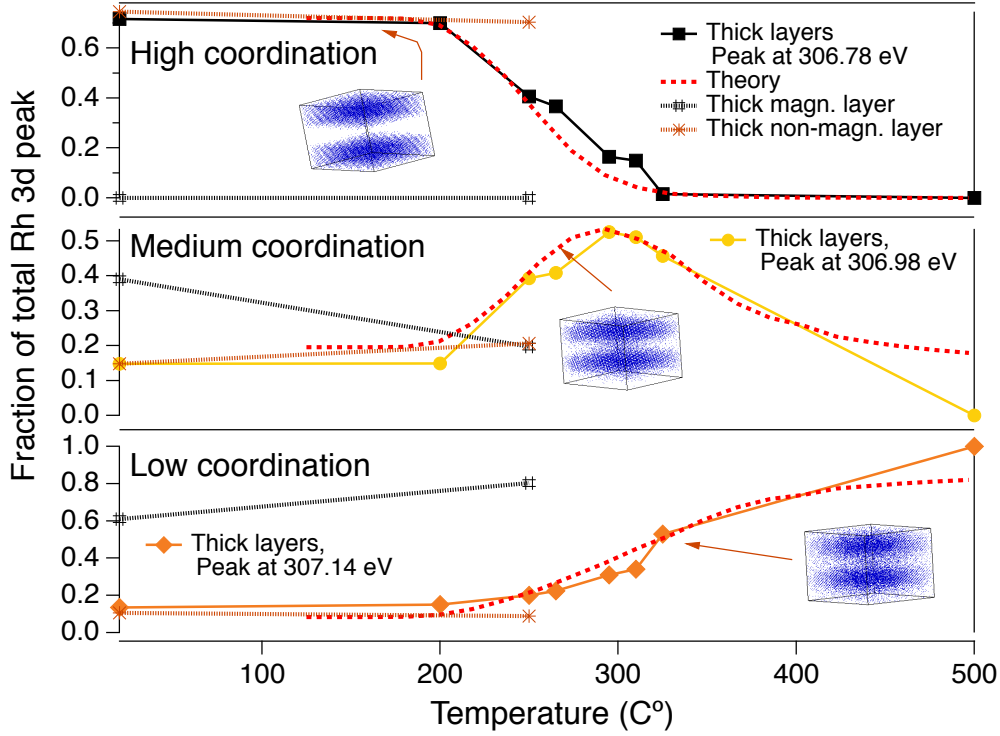


FIG. 3. (Color online) Fractions of the total peak areas of the Rh $3d_{5/2}$ core level spectrum, corresponding to the three main peaks obtained by fitting as illustrated in Fig. 2, are plotted as a function of annealing temperature. Top panel: high coordination component; middle panel: medium coordination component; bottom panel: low coordination component. Data for the three different samples considered are identified as indicated in the legends in each sub-panel. The dashed lines have been obtained from Monte Carlo simulations describing the variation of the high, medium and low coordination number cases with annealing temperature. The three lattice illustrations show the Rh distribution for different annealing temperatures.

where E is an energy barrier, for an atom to be allowed to move. It was enough to give every atom the opportunity to move 600 times at each temperature, since the simulation results became relatively insensitive to additional moves beyond this number. The energy scale (i.e. reduced temperature) of the simulation was scaled to the experimental results. In a perfectly layered structure the amount of low coordinated atoms should be zero. To obtain a more realistic starting configuration, a roughness corresponding to a displacement of randomly chosen Rh atoms at the interface, was introduced. To obtain agreement with experiments,

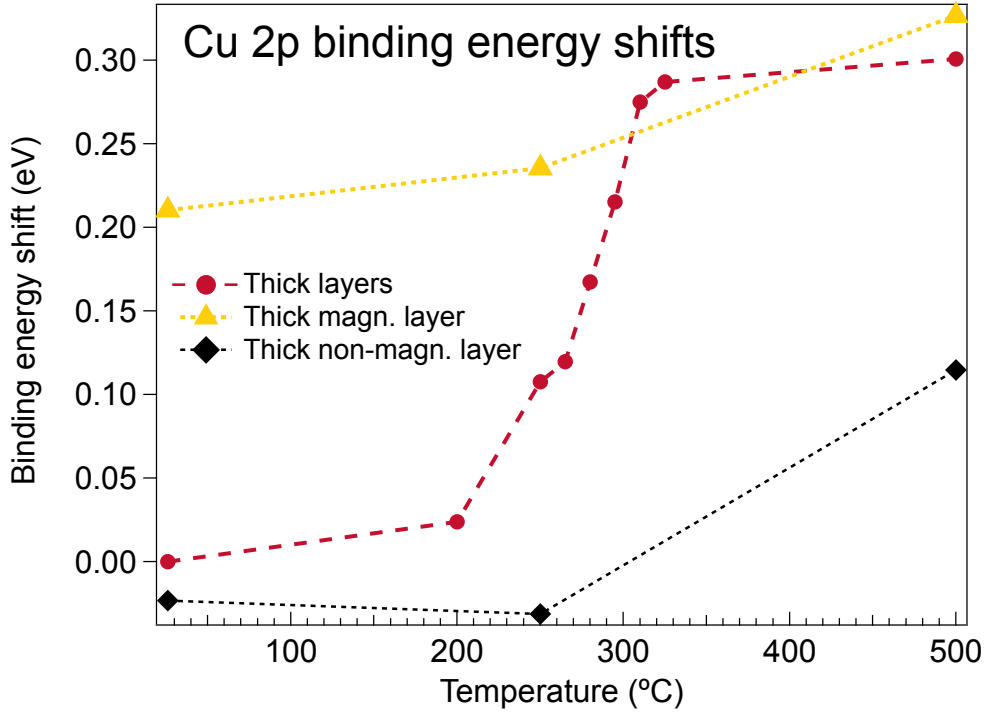


FIG. 4. (Color online) The Cu 2p core level shift as a function of annealing temperature for three samples as indicated by the legends. The BE shifts are given relative to the position of the 2p level for the “Thick layers” sample prior to annealing. Small shifts are found for samples with thick CMG layers (‘Thick layers’ and ‘Thick magn. layer’) already at 200 °C. We observe no chemical shift below 250 °C for the sample with the thick non-magnetic layers, suggesting little modification below this temperature.

we found that, on average, every fourth interface Rh atom had to be moved. Illustrations of how the multilayer composition according to the simulations changes with increasing annealing temperature have been included as insets in Fig. 3. The fractions of atoms with 12, 8-11 and 0-7 Rh neighbors are plotted as red dashed lines in the top, middle and bottom graphs, respectively. Using a combination of statistical methods and analysis of core level data we can thus obtain a qualitative and quantitative analysis of the distribution of Rh as a function of temperature. These results will be discussed further below, in connection to the presentation of data from the other core levels.

The Cu 2p core level spectra, obtained for different annealing conditions, do not exhibit

as large chemical shift as the Rh $3d_{5/2}$ core level and the spectrum is always broader (not shown). These factors makes it more difficult to use data for the Cu $2p$ level for quantitative analysis like for Rh as described above. By only considering the centroid of the spectrum fitted with a single Doniac-Sunjic profile, we can however assign chemical shift for each annealing temperature and sample. The result is presented in Fig. 4. The core level shift is given relative to the position of the $2p$ level for the "Thick layers" sample prior to annealing, which is thus set to zero. We observe that the sample with thick magnetic CMG layers and thin RCS layers exhibits a significant shift already before annealing. We therefore conclude that data for both the Cu and Rh core levels indicate that samples with a thin RCS layer have, as expected, a low fraction of ordered bulk-like RCS. In contrast we find that the BE of the Cu $2p$ core level for the sample with the thick RCS layer is very similar to the reference level of the "Thick layers" sample. Unlike the data for the Rh core level, the Cu core level data thus seems to indicate a higher degree of order for thinner magnetic layers. The temperature dependence of the Cu $2p$ core level shift for all three samples suggests that modifications occur already around 200°C . Especially we find that the core level shift of the "Thick layers" sample exhibit an abrupt transition in the temperature range 200°C - 300°C .

The Mn $2p$ spectra have been fitted by two peaks that both exhibit strong satellite structures, as illustrated in Fig. 5, where the results for the 'Thick layer' sample annealed at 250°C is shown. Also here, Shirley-type backgrounds were used. In the fitting procedure, the intensity of the satellite was kept constant relative to that of the main line. The main peak at $\sim 638.4\text{ eV}$ is attributed to the interior of the layer (bulk peak), while the peak at $\sim 638.6\text{ eV}$ is attributed to the interface. The fraction of each peak as a function of temperature is shown in Fig. 6. Similar to what was found for Cu above, there are also differences in the temperature dependence of the core level shift for the Mn $2p$ core level depending on the thickness of the adjacent layer. Also, as for Cu $2p$, we observe a changes for the Mn $2p$ core level already for an annealing temperature of 200°C . The bulk component is smaller for the 'Thick magnetic layer' sample which has a thinner RCS layer (triangles), which would suggest that the interface quality is lower for thinner RCS layers. As expected, the bulk component is also smaller for the 'Thick non-magnetic layer' sample with thinner CMG layer (diamonds).

In Fig. 7 we show both the chemical shift of the Co $2p_{3/2}$ core level and the spin magnetic moment of Co as obtained from an XMCD sum-rule analysis^{18,19}, as a function of annealing

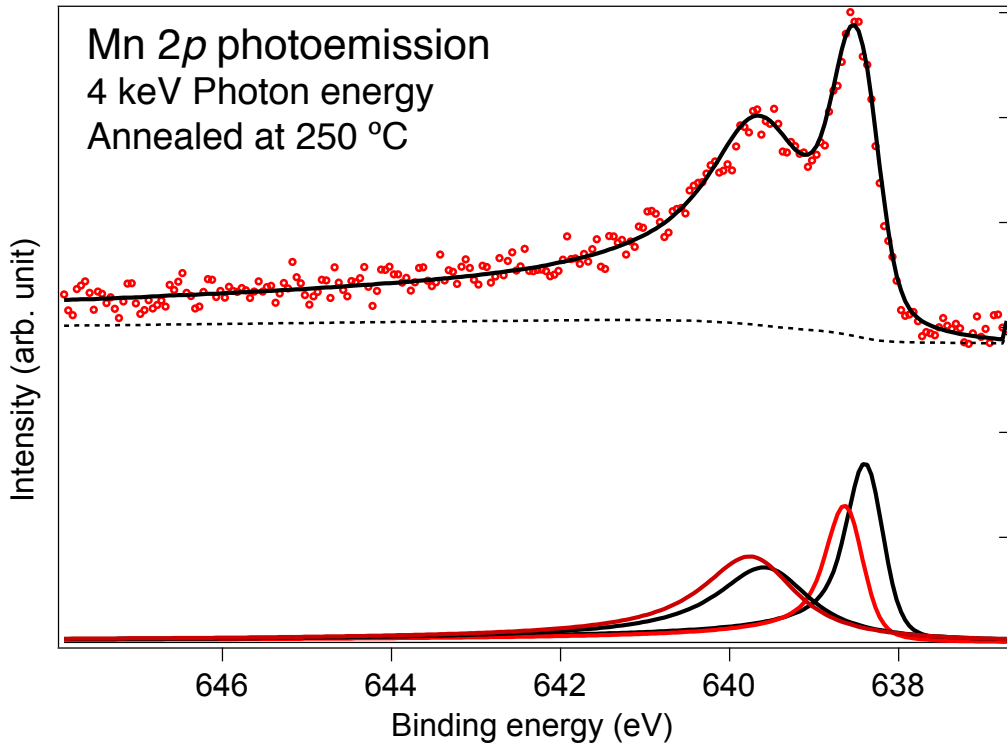


FIG. 5. (Color online) Deconvoluted Mn 2p spectrum recorded for the “Thick Layers” sample. The spectrum can be fitted by two components, and associated satellites, for all annealing temperatures. There is both a BE shift and a large difference in the satellite intensity between the components.

temperature. As for Cu, the core level shift was obtained by fitting a single Doniac-Sunjic line with a Shirley background to the data at each temperature and sample. The samples with thick CMG layers, i.e. the ‘Thick layers’ and ‘Thick magnetic layer’, exhibit a negligible chemical shift of the Co $2p_{3/2}$ core level up to 250 °C, suggesting little modification at the X sites below this temperature. Between 250 °C and 280 °C, we find an increasing positive shift. For an annealing temperature of 300 °C, the chemical shift becomes negative and we observe an increasing negative shift in the interval 300 °C - 330 °C. The qualitative behavior is very similar to the annealing temperature dependence of the spin magnetic moment obtained from the XMCD measurements, which also shows an increase in the same temperature range followed by a decrease. A 3d-hole count of 2.2 for Co and 4.2 for Mn^{28,29} was used for extracting the magnetic moment from the XMCD results using the sum rules^{18,19}. The formation of Co antisites, where Co atoms occupy Mn sites, or Mn antisites, where Mn

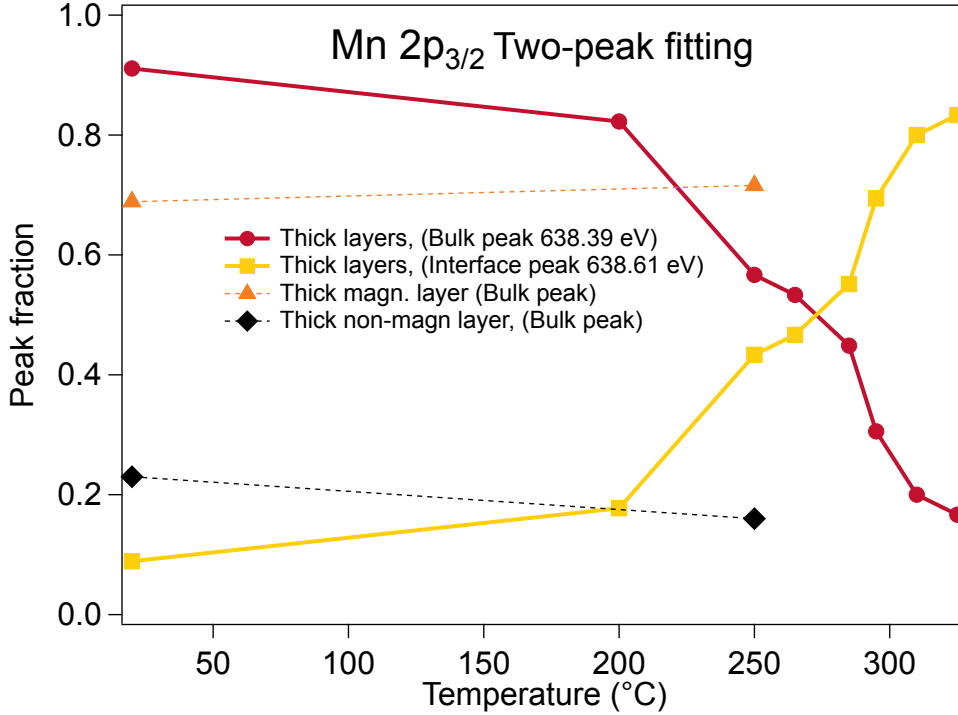


FIG. 6. (Color online) The intensity of the bulk (circles) and interface (squares) peaks, derived from fits like illustrated in Fig. 5, are plotted as a function of annealing temperature for the 'Thick layers' sample. Only the bulk component is plotted for the other samples (triangles and diamonds).

atoms occupy Co sites, are expected to occur in the FM Heusler layers^{11,16,30}. According to theory, Mn antisites will couple antiferromagnetically with its nearest neighbors, while for Co antisites there is instead an increase of the ferromagnetic moment by 32%.^{16,30} This could explain the observed increase of the Co moment, since we know that Mn is mobile already for an annealing temperature of 200 °C and it therefore becomes possible for Co to occupy Mn sites. One may note that Co antisites, unlike Mn antisites, are detrimental for the spin polarization of the material³⁰.

The sample consisting of 24 Å CMG/ 18 Å RCS was studied with neutron reflectivity to complement the spectroscopic methods. The sample was chosen due to its large layer thicknesses, which made it suitable for neutron reflectivity measurements. The data was analysed with the GenX program³¹ by co-refining all data sets up to 300 °C, keeping the same parameters for all temperatures except for the roughness of the RCS layer, CMG layer

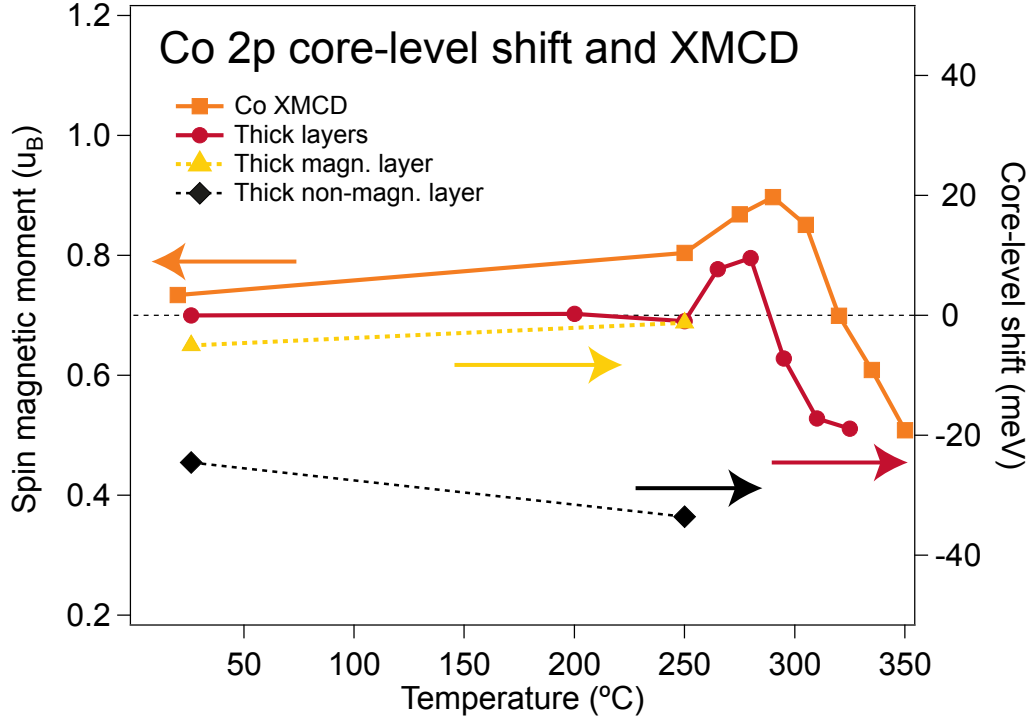


FIG. 7. (Color online) The Co XMCD spin magnetic moment is plotted on the left scale. On the right scale we have plotted the chemical shift of the Co $2p_{3/2}$ core level. The behavior of the chemical shift and magnetic moment is very similar.

and the capping layer. In addition, the magnetic moment for the CMG layer was allowed to vary. For the four refined data sets, up to a temperature of 250 °C, there was a total of 51 free parameters yielding a fit with a crystallographic R1 factor of 5.7 %. The results of the fits together with raw data can be seen in Fig. 8 (left). The resulting scattering length density (SLD) for the magnetic and nuclear scattering length are plotted with yellow and red colors, respectively. The substrate is located to the left in the plots and the film/air interface is located to the right. The parameters of interest in this study; the roughness of the multilayer interfaces and the magnetic moment of the CMG layer can be seen in Fig. 8 (right). It should be noted that after an anneal to 300 °C the multilayer Bragg peak has disappeared completely indicating a total intermixing of the layered structure (not shown). This temperature can consequently not be modelled by merely allowing the roughnesses to vary as there are no interfaces left, consequently it is left out of the discussion of the

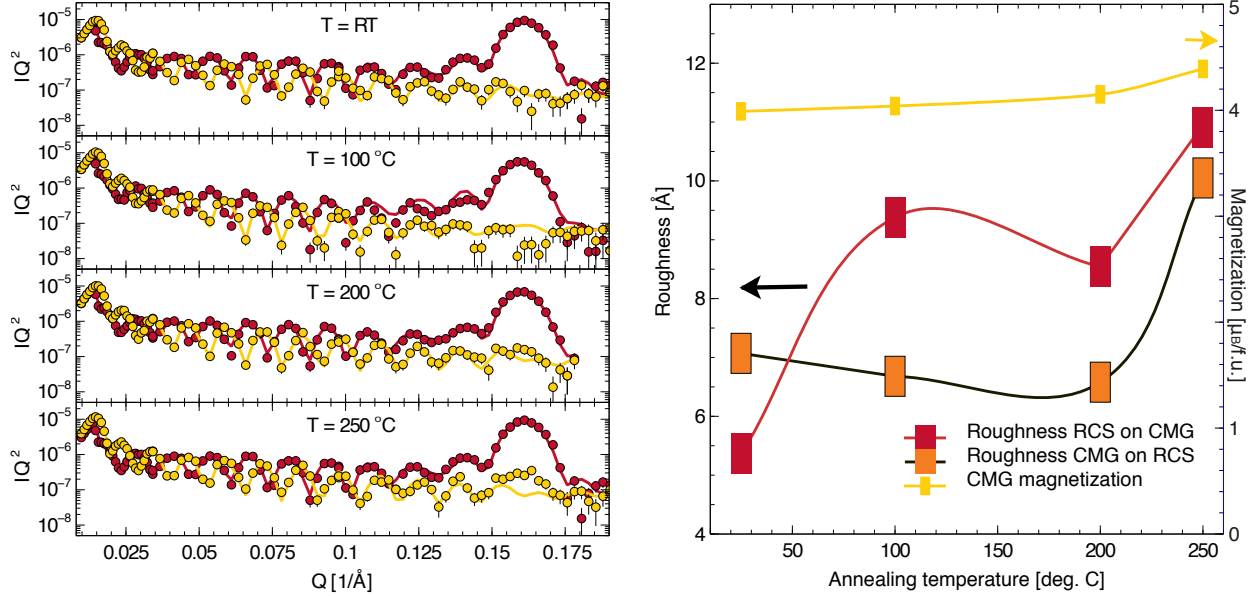


FIG. 8. (Color online) (left) Neutron reflectivity data where the scattering length density for the magnetic and nuclear scattering length are plotted with yellow and red colors, respectively. (right) The interface roughness and magnetic moment obtained from the refinement using GenX³¹. The roughness of RCS grown on CMG is very sensitive to annealing already at 100 °C.

reflectivity data. However, the large changes seen as the annealing temperature increases to 300 °C is in agreement with the HIKE data that also show layer interdiffusion at these temperatures. The first rise in the roughness of the RCS on CMG interface in Fig. 8 (right) is in accordance with the weak intermixing seen for the Mn and Cu core levels. The intermixing is mostly localized to one of the interfaces in the multilayer structure, RCS on CMG, and starts already at around a temperature of 100 °C. We again note the distinction between the protocols used for heating due to differences in the hardware used. The longer annealing time used for the samples used in the neutron measurements are likely giving rise to the apparent higher degree of interdiffusion indicated by the neutron data.

The saturation magnetic moments for all samples were obtained with SQUID magnetometry. The 6 Å CMG/ 18 Å RCS sample, which shows no remanence in XMCD, was used for providing the magnetization of the FeCo seed layer by assuming that only this layer contribute to the remanent magnetization obtained from the SQUID magnetometry. The magnetization of FeCo was found to be $1.5 \cdot 10^6$ A/m which is close to the bulk value of

$1.74 \cdot 10^6$ A/m.

To account for the magnetization obtained by means of SQUID magnetometry we find that it necessary to include magnetically dead layers in each CMG layer. If one assumes the theoretical magnetic moment of $5 \mu_B/f.u.$ in the CMG layer one finds that a magnetically dead layer needs to be included, to account for the measured magnetic moment. The thickness of this magnetically dead will have to increase from 5 to 10 Å as the CMG layer thickness increases from 12 to 24 Å. However, as illustrated in Fig. 9, if one assumes a magnetic moment of $4 \mu_B/f.u.$ we find that the required thickness of the dead layer is much less dependent on the CMG/RCS thickness, with an approximately constant thickness of about 4 Å. This corresponds well to the magnetic moment found by neutron reflectivity. In Fig. 9, the dead layer thickness for samples with 18 Å CMG and varying RCS layer is plotted as red circles. For samples with 18 Å RCS and varying CMG layer, the dead layer thickness is plotted as blue diamonds. A small increase in the dead layer thickness is found for samples annealed to 250 °C.

The XMCD Co spin magnetic moment as a function of CMG and RCS layer thicknesses are shown in Fig. 10. In the upper graph we give the data for a constant CMG layer thickness of 18 Å varying the RCS layer thickness, while for the lower graph we vary the CMG layer thickness keeping the RCS layer thickness constant at 18 Å. The black dashed line corresponds to the average Co moment in the CMG layer, assuming a 4 Å thick magnetically dead layer and a Co spin moment of $1\mu_B$ ^{32,33} in the remaining part of the CMG layer. In the lower graph we observe an increase of the magnetic moment with increasing CMG thickness. It should be explicitly noted that the 6 Å CMG sample does not show any XMCD signal. Assuming a 4 Å magnetically dead layer in CMG and a Co magnetic moment of $1 \mu_B$, we obtain a reasonable fit to the experiment results as indicated by the black dashed line in the lower graph of Fig. 10.

The Mn XMCD is hampered by large background contributions but a reliable spin magnetic moment could be derived for the sample with the thick magnetic layer. Moreover, using the sum rules for Mn is not straightforward due to mixing of the Mn L_2 and L_3 edges. A correction factor of 1.47 has been proposed³⁴. However, Saito et al.³³ found that omitting the correction factor gives more reasonable values of the Mn spin magnetic moment. Taking the 4 Å magnetically dead layer in consideration we obtain a Mn spin magnetic moment of $1.98 \mu_B$ without considering a correction factor. This gives a total magnetic moment of

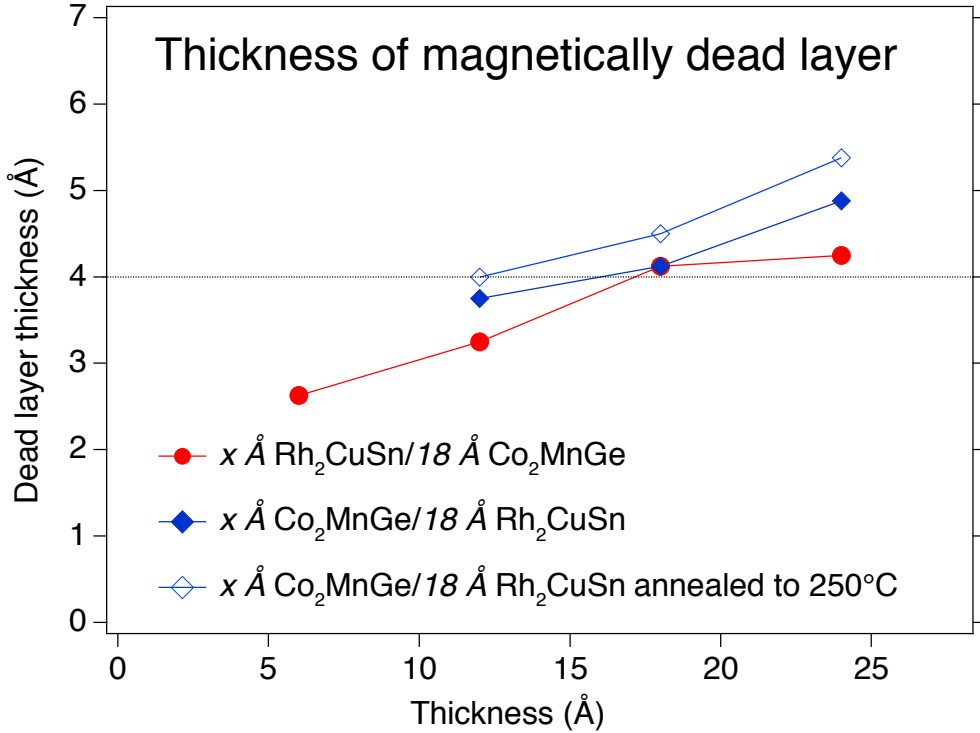


FIG. 9. (Color online) Estimated thickness of the magnetically dead layer for different layer thicknesses obtained from SQUID magnetometry. (Red circles) The thickness for the CMG layer has been kept constant at 18 Å, while the RCS layer thickness is varied between 6-24 Å. (Solid blue diamonds) The RCS layer thickness is 18 Å, while the CMG thickness is varied between 12-24 Å. (Unfilled blue diamonds) As previous data, but the samples have been annealed at 250 °C. The dead layer thickness is relatively insensitive to the thickness of the layers.

3.93 μ_B in the unit cell, which is very close to the magnetic moment obtained from neutron reflectivity. Others studies have found that the magnetic moment of Co increases for thin layers compared to bulk while the Mn is generally smaller^{32,33}. This can be explained by the disorder in thin films giving an increased magnetic moment for Co_{Mn} while Mn_{Co} is antiferromagnetically coupled to its nearest neighbors and will hence lower the saturation magnetization of the film.³⁰

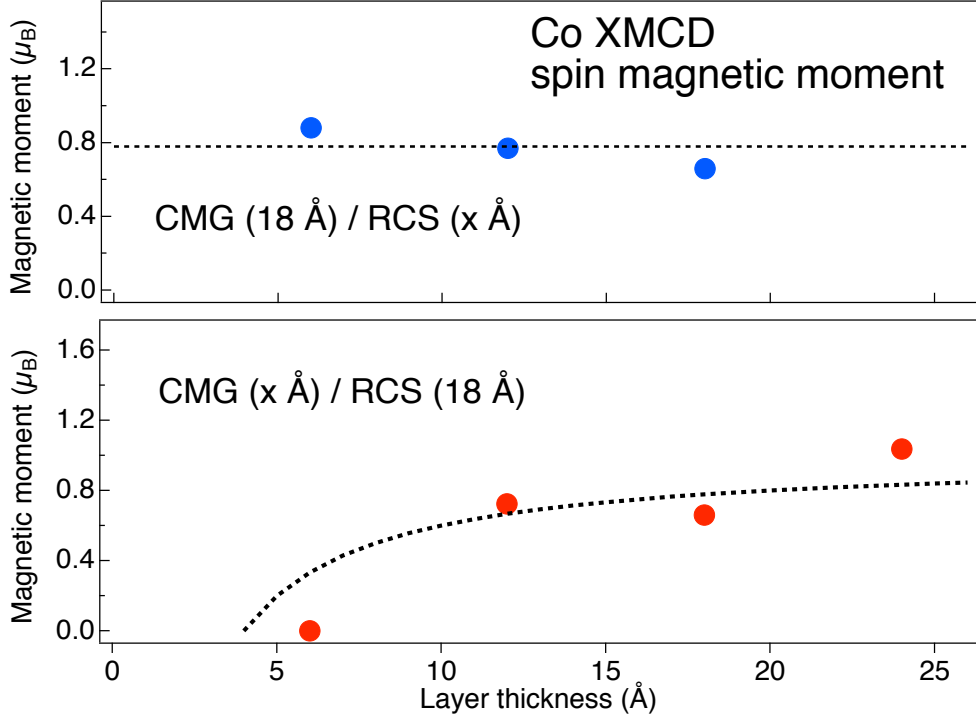


FIG. 10. (Color online) The Co spin magnetic moment for different CMG and RCS layer thicknesses before annealing. The top graph shows data for a constant CMG layer thickness of 18 \AA varying the RCS layer thickness, while the lower graph shows data for a constant RCS layer thickness of 18 \AA varying the CMG layer thickness. The increase of the magnetic moment in the lower graph indicates a 4 \AA thick magnetically dead layer in the CMG layers.

IV. CONCLUSIONS

The core levels of Mn and Cu indicate weak intermixing of the CMG and RCS layers already for an annealing temperature of 200 $^{\circ}\text{C}$, while for annealing temperatures above 250 $^{\circ}\text{C}$ we observe significant changes for all studied core-levels. We have shown that the Co atoms in the Co_2MnGe layer appear to be relatively immobile for annealing temperatures below 250 $^{\circ}\text{C}$, while for higher annealing temperatures Co antisites are created. These antisites have a negative impact on the spin polarization of the material. Varaprasad et al.²⁷ showed that the amount of Co antisites can be reduced by exchanging 25% of the Ge with Ga. The increase of the Co magnetic moment with increasing CMG layer thickness can

be explained reasonably well by assuming a 4 Å magnetically dead layer in CMG. The total magnetization of CMG is about $4 \mu_B$ which is lower than the bulk value of $5 \mu_B$. This is likely due to Mn_{Co} antisites which couple anti-ferromagnetically to their nearest neighbors, while Co_{Mn} antisites would give an increase in magnetic moment. Both Co and Rh, i.e. the A site atoms in two different layers, appear insensitive to the thickness of the adjacent layer before annealing. Rh has about 10% of the atoms in a low coordinated state before heat treatment which is in accordance with neutron reflectivity data suggesting a roughness of 6 Å at the interfaces. Furthermore, the interface where RCS is grown on CMG appears to be sensitive to heat treatments below 250 °C. Our findings has profound consequences for applications based on these materials, since actual devices are annealed at 250 °C during fabrication.

ACKNOWLEDGMENTS

This work was supported by the Swedish Research Council (VR) and the Swedish Foundation for International Cooperation in Research and Higher Education (STINT). VR is also acknowledged for their financial support of SuperAdam. We acknowledge the Helmholtz-Zentrum Berlin - Electron storage ring BESSY II for provision of synchrotron radiation at beamline KMC-1. We also would like to thank M.Mertin for assistance. The research leading to these results has received funding from the European Community's Seventh Framework Programme (FP7/2007-2013) under grant agreement n. °226716. Olof Karis gratefully acknowledge the support of the Göran Gustavsson Foundation.

-
- ¹ M. Baibich, J. Broto, A. Fert, F. Vandau, F. Petroff, P. Eitenne, G. Creuzet, A. Friederich, and J. Chazelas, *Phys. Rev. Lett.* **61**, 2472 (1988).
 - ² G. Binasch, P. Grünberg, F. Saurenbach, and W. Zinn, *Phys. Rev. B* **39**, 4828 (1989).
 - ³ M. Takagishi, K. Yamada, H. Iwasaki, H. N. Fuke, and S. Hashimoto, *IEEE Transactions on Magnetism* **46**, 2086 (2010).
 - ⁴ R. A. de Groot, F. M. Mueller, P. G. v. Engen, and K. H. J. Buschow, *Phys. Rev. Lett.* **50**, 2024 (1983).

- ⁵ M. I. Katsnelson, V. Y. Irkhin, L. Chioncel, A. I. Lichtenstein, and R. A. de Groot, *Rev. Mod. Phys.* **80**, 315 (2008).
- ⁶ J. Caballero, Y. Park, J. Childress, J. Bass, W. Chiang, A. Reilly, W. Pratt, and F. Petroff, *J. Vac. Sci. & Techn. A-Vacuum Surfaces and Films* **16**, 1801 (1998).
- ⁷ T. Iwase, Y. Sakuraba, S. Bosu, K. Saito, S. Mitani, and K. Takanashi, *Appl. Phys. Expr.* **2**, 063003 (2009).
- ⁸ T. M. Nakatani, T. Furubayashi, S. Kasai, H. Sukegawa, Y. K. Takahashi, S. Mitani, and K. Hono, *Appl. Phys. Lett.* **96**, 212501 (2010).
- ⁹ T. Ambrose and O. Mryasov, “Half-metallic alloys: Fundamentals and applications,” (Springer Verlag, Berlin-New York, 2005).
- ¹⁰ T. Ambrose and O. Mryasov, U.S. Patent No. 6,876,522 (5 April 2005).
- ¹¹ K. Nikolaev, P. Kolbo, T. Pokhil, X. Peng, Y. Chen, T. Ambrose, and O. Mryasov, *Appl. Phys. Lett.* **94**, 222501 (2009).
- ¹² J. Sato, M. Oogane, H. Naganuma, and Y. Ando, *Appl. Phys. Expr.* **4**, 113005 (2011).
- ¹³ M. Carey, et al, *Appl. Phys. Lett.* **85**, 4442 (2004).
- ¹⁴ K. Ozdogan and I. Galanakis, *J. Appl. Phys.* **110**, 076101 (2011).
- ¹⁵ I. Galanakis, K. Oezdogan, and E. Sasioglu, in *Advances In Nanoscale Magnetism*, Springer Proceedings in Physics, Vol. 122 (Springer-Verlag, Berlin, Germany, 2009) p. 328.
- ¹⁶ B. Ravel, J. Cross, M. Raphael, V. Harris, R. Ramesh, and V. Saraf, *Appl. Phys. Lett.* **81**, 2812 (2002), cited By (since 1996) 47.
- ¹⁷ M. Lezaic, P. Mavropoulos, S. Bluegel, and H. Ebert, *Phys. Rev. B* **83**, 094434 (2011).
- ¹⁸ P. Carra, B. T. Thole, M. Altarelli, and X. Wang, *Phys. Rev. Lett.* **70**, 694 (1993).
- ¹⁹ B. T. Thole, P. Carra, F. Sette, and G. van der Laan, *Phys. Rev. Lett.* **68**, 1943 (1992).
- ²⁰ E. Holmström, W. Olovsson, I. Abrikosov, A. Niklasson, B. Johansson, M. Gorgoi, O. Karis, S. Svensson, F. Schäfers, W. Braun, G. Öhrwall, G. Andersson, M. Marcellini, and W. Eberhardt, *Phys. Rev. Lett.* **97**, 266106 (2006).
- ²¹ S. Granroth, R. Knut, M. Marcellini, G. Andersson, S. Svensson, O. Karis, M. Gorgoi, F. Schäfers, W. Braun, W. Eberhardt, W. Olovsson, E. Holmström, and N. Mårtensson, *Phys. Rev. B* **80**, 094104 (2009).
- ²² M. Gorgoi, S. Svensson, F. Schäfers, G. Öhrwall, M. Mertin, P. Bressler, O. Karis, H. Siegbahn, A. Sandell, H. Rensmo, W. Doherty, C. Jung, W. Braun, and W. Eberhardt, *Nuclear Instru-*

ments and Methods in Physics Research Section A: Accelerators, Spectrometers, Detectors and Associated Equipment **601**, 48 (2009), special issue in honour of Prof. Kai Siegbahn.

- ²³ R. Knut *et al.*, To be published.
- ²⁴ B. Johansson and N. Mårtensson, Phys. Rev. B **21**, 4427 (1980).
- ²⁵ S. Doniach and M. Sunjic, J. Phys. C: Solid State Physics **3**, 285 (1970).
- ²⁶ J. Végh, Journal of Electron Spectroscopy and Related Phenomena **151**, 159 (2006), and references therein.
- ²⁷ B. Varaprasad, A. Rajanikanth, Y. Takahashi, and K. Hono, Appl. Phys. Exp. **3**, 023002 (2010).
- ²⁸ V. N. Antonov, O. Jepsen, A. N. Yaresko, and A. P. Shpak, J. Appl. Phys. **100** (2006).
- ²⁹ J. Grabis, A. Bergmann, A. Nefedov, K. Westerholt, and H. Zabel, Phys. Rev. B **72**, 024437 (2005).
- ³⁰ S. Picozzi, A. Continenza, and A. J. Freeman, Phys. Rev. B **69**, 094423 (2004).
- ³¹ M. Björck and G. Andersson, J. Appl. Crystallogr. **40**, 1174 (2007).
- ³² D. Asakura, T. Koide, S. Yamamoto, K. Tsuchiya, T. Shioya, K. Amemiya, V. R. Singh, T. Kataoka, Y. Yamazaki, Y. Sakamoto, A. Fujimori, T. Taira, and M. Yamamoto, Phys. Rev. B **82**, 184419 (2010).
- ³³ T. Saito, T. Katayama, T. Ishikawa, M. Yamamoto, D. Asakura, T. Koide, Y. Miura, and M. Shirai, Phys. Rev. B **81**, 144417 (2010).
- ³⁴ Y. Teramura, A. Tanaka, and T. Jo, J. Phys. Soc. Jpn. **65**, 1053 (1996).